High Temperature Corrosion of Materials (2026) 103:16
https://doi.org/10.1007/s11085-025-10365-z

RESEARCH

Kinetics and oxide morphology of chromium–tantalate formation on a model alloy Cr-20Ta in low oxygen partial pressure

F. Lanoy[1] · E. M. H. White[1] · B. Schäfer[2] · C. Tang[2] · C. Schroer[2] · M. T. Duerrschnabel[2] · B. Gorr[2] · M. C. Galetz[1]

Received: 2 September 2025 / Revised: 12 November 2025 / Accepted: 1 December 2025

Abstract
This study investigates the oxidation behavior of a binary Cr-20 at.%Ta alloy in a nitrogen-free, reduced oxygen partial pressure environment at 1000 °C for 48 h, aiming to clarify the intrinsic formation and growth mechanisms of protective (Cr, Ta)O_2 oxides. Chromium outward diffusion primarily governs oxidation, leading to a duplex scale with an outer Cr_2O_3 layer and an inner (Cr,Ta)O_2 subscale. Two distinct (Cr, Ta)O_2 phases were identified: $CrTaO_4$ (rutile structure) in outer regions and $CrTa_2O_6$ (trirutile structure) closer to the substrate, with $CrTa_2O_6$ confirmed as thermodynamically more stable through post-oxidation heat treatment and calculations. Thermogravimetric analysis revealed the parabolic oxidation constant of Cr-20 at.%Ta for fine-grained samples was eight times lower than pure chromium, highlighting the beneficial effect of the (Cr, Ta)O_2 layer. The microstructure significantly influences the protectiveness: fine-grained alloys promoted a continuous (Cr, Ta)O_2 layer, leading to enhanced oxidation resistance, particularly after a transient period required for the protective subscale to establish. This research underscores the critical role of (Cr, Ta)O_2 and microstructure in developing advanced oxidation-resistant refractory alloys.

Keywords Refractory alloys · High-temperature oxidation · Chromium-tantalate · Microstructure · Laves phase

Introduction

Refractory alloys are gaining increased attention in search of materials that can withstand temperatures beyond the operational capabilities of Ni-based alloys. One major challenge that all refractory metals share is their inability to grow protective oxides [1]. At temperatures as low as 500 °C, and thus well below their target

Extended author information available on the last page of the article

Published online: 31 January 2026

application temperatures, Nb, Ta or Mo begins to oxidize catastrophically by the formation of either voluminous or volatile oxides, both resulting in unfavorable linear weight changes.

Recently, high entropy (or compositionally complex) refractory alloys [2–6] have been identified as high temperature structural material candidates [3–9]. They offer significantly higher strengths than conventional alloys [10, 11], but their oxidation resistance remains insufficient in most cases. On several such systems, rutile-structured $(Cr,Ta)O_2$ has been identified to form as an oxide layer, with an ascribed potential to increase the high temperature oxidation resistance significantly [3–6].

These $(Cr,Ta)O_2$ oxides have been shown to form continuous layers that contribute to relatively slow-growing scales in various alloys [3–6, 12]. Their presence was also reported for nickel-based superalloys as part of more complex oxide scales [13–15]. Experiments have shown that when other oxides were removed and only $(Cr,Ti,Ta)O_2$ remained on the surface of CCAs after oxidation, this scale remains stable during subsequent high temperature exposure [4]. Butler et al. suggested that the interplay with a second protective layer, such as chromia, is required for the slow growth of such $(Cr,Ta)O_2$ scales [16]. These observations affirm that $(Cr,Ta)O_2$ can be a key compound for the oxidation resistance of new refractory metal alloys, but also show that its role is complex in multicomponent alloy systems.

The goal of this study is to investigate the formation mechanism and growth kinetics of pure $(Cr,Ta)O_2$ scale using a model Cr-20 at.%Ta alloy. This eliminates the influence of other alloying elements on the formation of potentially protective $(Cr,Ta)O_2$. Additionally, previous studies were limited to high temperature oxidation in nitrogen-containing atmospheres [3–6, 16–23] and concluded that nitridation competes with $(Cr,Ta)O_2$ formation, as CrN forms a subscale [17, 18]. For this study, a nitrogen-free atmosphere at a reduced oxygen partial pressure was chosen, as studies have shown that a reduced oxygen partial pressure promotes the formation of adherent, slow-growing (parabolic kinetics) $(Cr,Ta)O_2$ scales [19, 21] and minimizes the potential impact of Cr evaporation. Nitrogen-free, low oxygen partial pressure environments have not been addressed in previous work [3, 5–8, 17–21, 23–27]. Eliminating nitrogen from the atmosphere simplifies the system and enables the investigation of the inherent properties of $(Cr,Ta)O_2$ and their resulting growth kinetics. Additionally, samples with finer microstructures have been investigated to evaluate the influence of the microstructure on the protectiveness of $(Cr,Ta)O_2$ scales, which can be quite significant [16].

Experimental Procedures

Sample Manufacturing

The first sample material was manufactured by arc-melting (Edmund Bühler AM500) high-purity (>=99.9%) raw materials (Haines-Maassen, QUKEN) in argon according to the desired chemical composition of 80 at.% Cr and 20 at.% Ta to produce ~100 g buttons. The second material was manufactured as a series of smaller-scale samples and produced by arc melting smaller batches (~2 g per

sample, Edmund Bühler MAM-1) to result in a significantly finer dendritic microstructure. To remove segregation and homogenize the microstructure, all samples were heat treated at 1200 °C for 100 h in an argon atmosphere in a tube furnace (Nabertherm) with a flow rate of 0.5 L/h.

The resulting sample material was cut into smaller pieces (4 × 4 × 10 mm) using wire electric discharge machining, and all surfaces were ground to P1200 grit with SiC abrasive paper. Before oxidation, the material was ultrasonically cleaned in ethanol, weighed, and the surface area determined using image processing.

Oxidation

Individual samples were positioned in alumina crucibles in either a tube furnace (Nabertherm) for isothermal exposure or a vertical thermogravimetric analysis (TGA) furnace (DFI built) to determine the sample mass change during oxidation. Both experiments were performed at 1000 °C for 48 h in flowing Ar-2.5 vol.%O_2 (0.5 L/h). The residual nitrogen content of the utilized gases with $pN_2 = 4.9 \times 10^{-6}$ bar was four orders of magnitude smaller than the oxygen partial pressure of the gas, thus nitridation should play an neglectable role during the oxidation and heat treatment, according to thermodynamical calculations using FactSage 5 [28].

Post-Oxidation Heat Treatment

To assess the thermodynamic stability of the thermally grown oxides without further oxidation or oxygen uptake, a selected set of oxidized samples was subjected to a post-oxidation heat treatment in an inert, high purity Ar atmosphere at 1000 °C for 48 h to investigate if the existing scale remains stable in equilibrium with the underlying substrate.

Analysis

Sample surfaces were gold-coated via physical vapor deposition (PVD) and nickel-electroplated to protect the formed oxide layers during mounting in a conductive epoxy resin and subsequent grinding of metallurgical cross-sections. The mounted samples were polished using SiC abrasive paper up to P2400 grit, followed by 3 µm, 1 µm, and 20 nm diamond polishing suspension. The oxide scales were investigated microscopically in cross-sections using scanning electron microscopy (SEM, Hitachi FlexSEM 1000) in backscatter electron mode (BSE) to provide micrographs of the oxide layers. Electron probe microanalysis (EPMA, JEOL JXA-8100) was employed for quantitative chemical compositions and qualitative elemental maps using wavelength-dispersive spectroscopy (WDS) with standard-related calibration. Electron backscatter diffraction (EBSD, Hitachi SU5000) was used for high-resolution crystallographic information and to differentiate different phases locally. Phase identification was also performed using Micro-Raman-spectroscopy (Renishaw inVia, 633 nm), transmission electron microscopy (TEM, Thermofischer Talos F200X G2, SEAD) and X-ray diffraction (XRD, Bruker D8, Cu x-ray tube). Oxide thicknesses

were measured on SEM-BSE images using the image processing software Fiji [29]. They were performed in multiple regions of the samples with a minimum number of 20 measurements for statistical significance.

Results

Coarse Microstructure

After homogenization, the alloy exhibits a two-phase microstructure, as shown in Fig. 1, consisting of a dendritic Cr_2Ta C14 hexagonal intermetallic Laves phase and a A2 body-centered cubic Cr(Ta) solid solution. Both phases were identified via XRD (Fig. 1) and EBSD (not shown). The overall chemical composition, as determined by EPMA-WDS grid measurements of 100 points, was (79.9 ± 0.1) at.% Cr and (20.1 ± 0.1) at.% Ta. On average, the Cr solid solution has a composition of (95.9 ± 1) at.% Cr and (4.1 ± 1) at.% Ta. The C14 intermetallic Laves phase has a Cr content of (68.8 ± 0.1) at.% and (31.2 ± 0.1) at.% Ta. The volume fraction of the C14 Laves phase was determined to be (57 ± 5) vol.% using image area analysis. This microstructure and the compositions are in line with the results described before for the binary system [27].

Oxidation

Thermogravimetric Analysis

Figure 2 shows the results from the thermogravimetric analysis (including the fine microstructure described later). The equation describing parabolic mass gain (1) is fitted to this data using a least-squares algorithm to determine the parabolic oxidation constant, k_P.

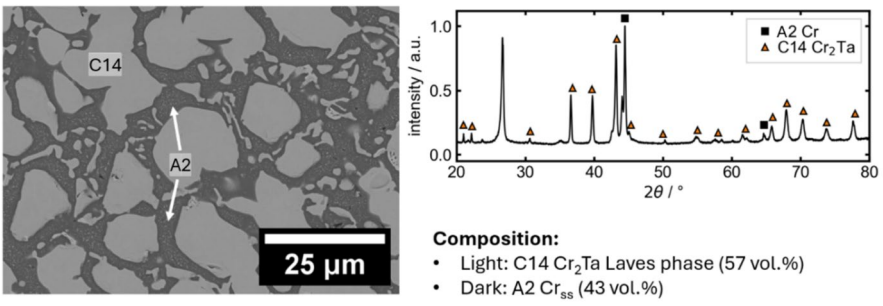

Fig. 1 SEM BSE micrograph (left) of annealed coarse Cr-20Ta, consisting of a C14 Laves phase with the composition Cr_2Ta (lighter areas) and A2 Cr(Ta) solid solution (darker areas). XRD pattern (right) confirms both A2 and C14 phases (unlabeled peaks are assigned to the mounting material)

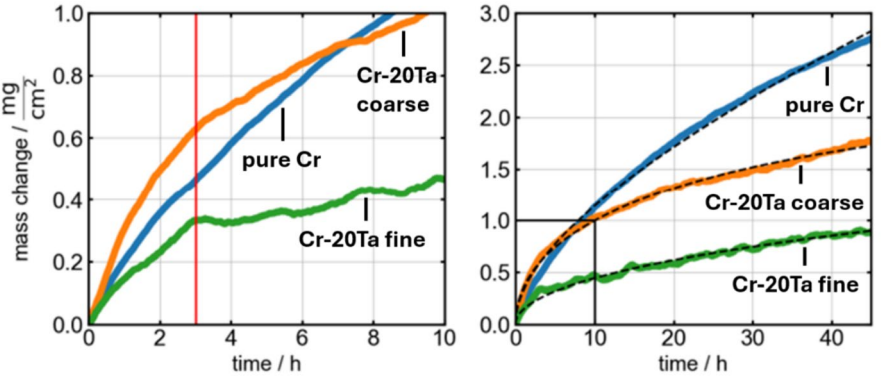

Fig. 2 Area-specific mass change of Cr-20Ta samples during oxidation compared to pure Cr. The Cr-20Ta samples have two different dendritic microstructures: coarse and fine. The dashed line represents the fitted curves. The left image is the enlarged initial period, as shown in the right image. Oxidations are performed at 1000 °C for 48 h in Ar-2.5 vol.%O_2

$$(\Delta m/A)^2 = k_P * t \tag{1}$$

The parabolic growth constant k_P are shown in Table 1 for pure Cr, coarse Cr-20Ta, and fine Cr-20Ta at 1000 °C for 48 h in Ar-2.5 vol.%O_2. Figure 2 also shows the fitted curves as dashed lines and their agreement with the measured mass gain data. These fits support the assumption that mass gain is predominantly parabolic. Figure 2 also shows the initial period enlarged, at 3 h, where both Cr-20Ta alloys initially exhibit a faster mass change, but the slope of their mass gain appears to change, indicating a slower oxide growth rate after 3 h.

A chromium oxide scale formed on the pure chromium, which does not spall off in this nitrogen-free atmosphere, while it usually spalls in air [33] (Fig. 3). On the coarser Cr-20Ta substrate, the oxide formation is more complex with a duplex scale in some areas and internal oxidation as well as nitrides in the subsurface zone, as shown in the BSE-SEM images in Fig. 4. Based on EPMA-WDS measurements, the phases in the duplex layer match the compositions of Cr_2O_3 (darker, outer layer) and (Cr,Ta)O_2 (brighter, inner layer) in Fig. 5. For the (Cr,Ta)O_2 layer, two phases were identified: $CrTaO_4$ and $CrTa_2O_6$. In this work, the term (Cr,Ta)O_2 is used to refer to both compositions, while $CrTaO_4$ and $CrTa_2O_6$ are used to differentiate and specify the exact compositions. Most spot measurements performed via EPMA-WDS (Fig. 5) indicated a chemical composition of $CrTa_2O_6$ further within the scale, while the outer regions in

Table 1 Parabolic mass gain coefficient as determined by TGA curve fitting after oxidation at 1000 °C for 48 h in Ar-2.5%O_2

Sample material	$k_P/g^2\ cm^{-4}\ h^{-1}$
Pure chromium	$1.6 * 10^{-7}$
Coarse Cr-20Ta	$7.7 * 10^{-8}$
Fine Cr-20Ta	$1.8 * 10^{-8}$

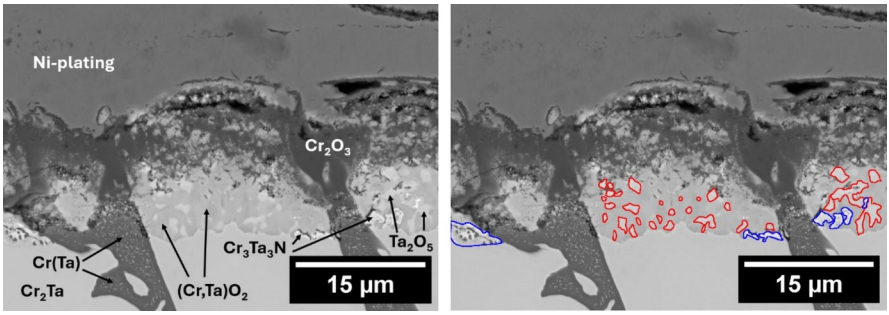

Fig. 3 Cross-sectional SEM-BSE of the oxide layer and underlying substrate after oxidation of Cr-20 at.%Ta (1000 °C for 48 h in Ar-2.5 vol.%O_2). In the right image, Ta-oxide inclusions are highlighted in red and Cr_3Ta_3N in blue

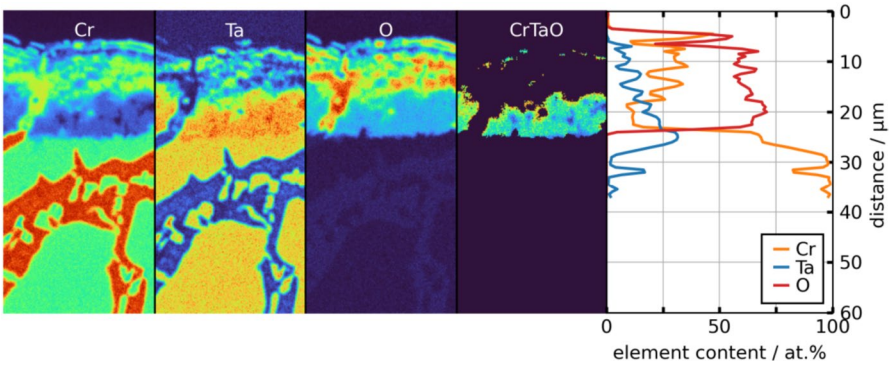

Fig. 4 EPMA-WDS elemental maps of Cr, Ta, and O and an overlay to highlight (Cr,Ta)O_2 after oxidation (1000 °C for 48 h in Ar-2.5 vol.%O_2). The right graph shows the quantitative line-scan depth profile with $CrTaO_4$ in the upper region and $CrTa_2O_6$ deeper within the oxide

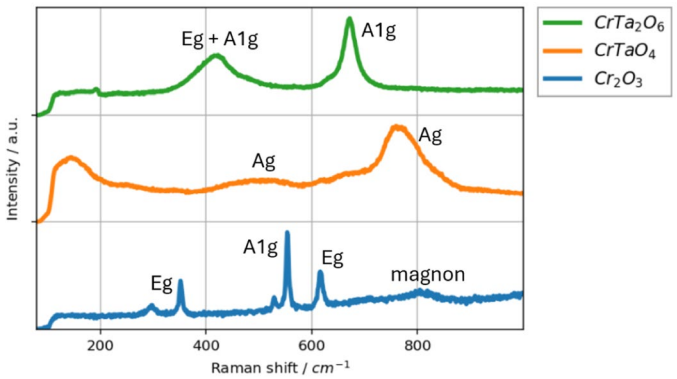

Fig. 5 Raman spectra of the formed oxides in the scale of a Cr-20Ta sample with a coarse microstructure (1000 °C for 48 h in Ar-2.5 vol.%O_2). Vibrations corresponding to the peaks are identified and labeled [30–32]

contact with Cr_2O_3 matched a composition corresponding to $CrTaO_4$. $CrTa_2O_6$ exhibits a trirutile-type crystal structure, as confirmed by micro-Raman spectroscopy, see Fig. 3. The $CrTaO_4$, on the other hand, has a rutile crystal structure. In the BSE-SEM image of Fig. 4, both $(Cr,Ta)O_2$ phases appear as a lighter area visible within the oxide region. Both $(Cr,Ta)O_2$ phases are solely formed on the Laves dendrites, not on the Cr solid solution, which is in line with other studies [6, 27] (Fig. 6). Locally, internal oxidation of Ta_2O_5 and a N-lean nitride of Cr_3Ta_3N was observed at the interface between the oxide and substrate. Such minor amounts of transformed Laves phase present under the $(Cr,Ta)O_2$ and sporadically within the sample were not distinguishable from the surrounding C14 Laves phase using XRD and EBSD. To identify such phases, TEM analysis (Fig. 7) with STEM-EDS indicated 14.7 at.% of nitrogen in the transformed regions, the results of which are shown in Table 2. Selected area electron diffraction analysis confirmed this transformed phase to be Cr_3Ta_3N, and the chemical composition approximately fits this compound, see Table 2.

Using EPMA-WDS (Fig. 5) and high resolution EDS (Fig. 8), Ta_2O_5 was distinguishable from the surrounding oxide and nitride with a similar BSE-SEM contrast, with oxygen present, but Cr dissolution being low in Ta_2O_5. The

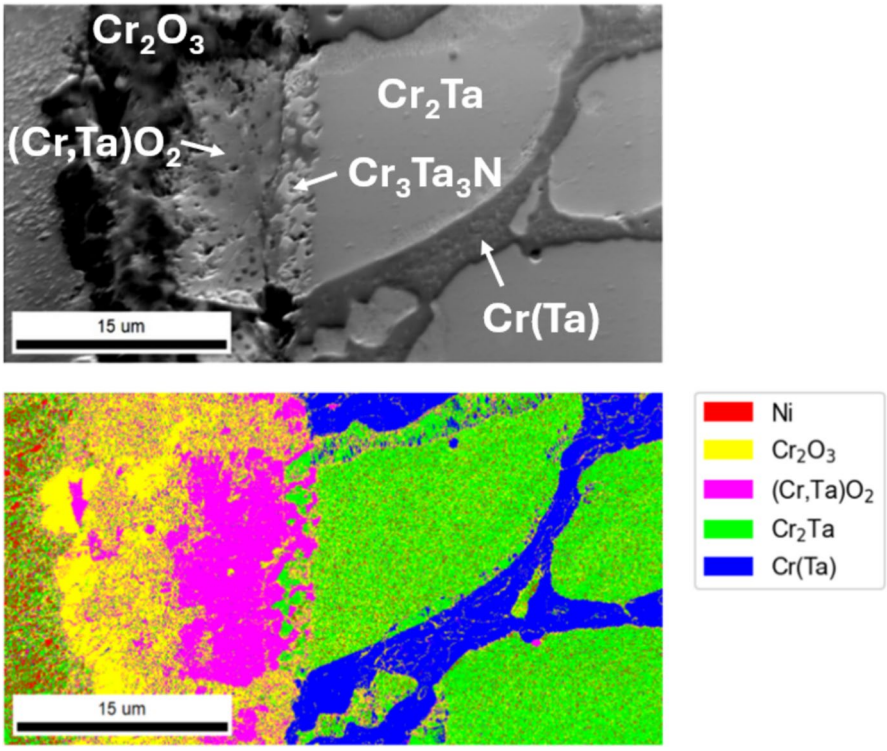

Fig. 6 SEM-SE and EBSD images after oxidation (1000 °C for 48 h in Ar-2.5 vol.%O_2); color-coded areas show the identified phases. The rutile structures of $CrTaO_4$ and $CrTa_2O_6$ could not be differentiated via EBSD and are labeled as $(Cr,Ta)O_2$

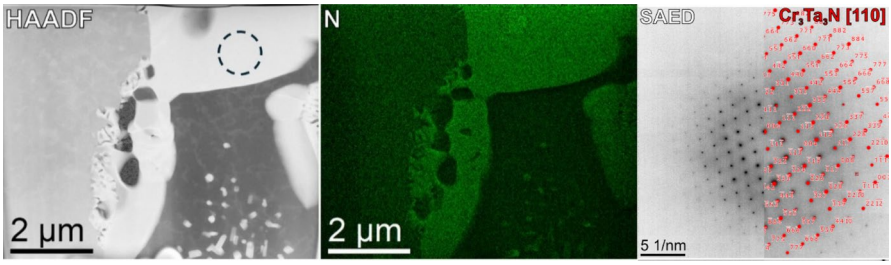

Fig. 7 STEM EDS and SEAD images of the lighter transformed phase at the oxide-substrate interface (1000 °C for 48 h in Ar-2.5 vol.%O_2). Selected area electron diffraction (SAED) and EDS suggest the phase to be Cr_3Ta_3N. The dashed circle represents the SEAD area

Table 2 STEM EDS elemental analysis results of the light and precipitate-rich transformed phase

at.%	Cr	Ta	N
EDS-quantification	47.2 ± 3.9	38.1 ± 3.5	14.7 ± 1.1

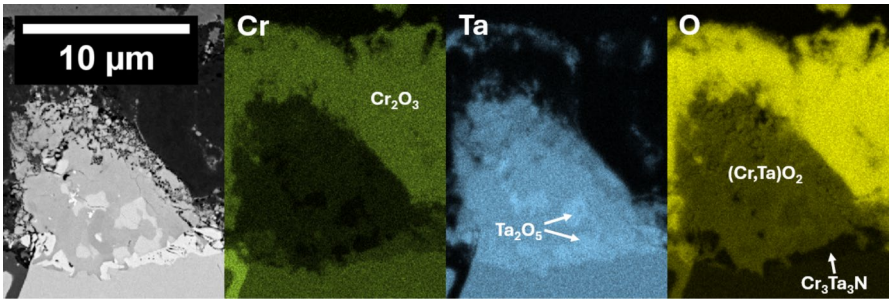

Fig. 8 High resolution BSE and EDS elemental maps of the oxide-substrate interface region showing Cr_3Ta_3N at the interface, Ta_2O_5 within the $(Cr,Ta)O_2$ and nitride below after oxidation at 1000 °C for 48 h in Ar-2.5 vol.%O_2

Cr_3Ta_3N phase has a lower Cr content than the original Cr_2Ta Laves phase, but is oxygen-free, enabling distinction between these phases, as seen in Fig. 8.

Qualitative EPMA maps, as shown in Fig. 5, also revealed that no significant oxygen was taken up into the metal underneath the oxides. SEM-EBSD (Fig. 6) confirmed the chromium tantalum oxides at the chromia/Laves phase interface but was unable to differentiate between the two similar rutile structures.

Interestingly, areas where the microstructure was transformed were also found deeper within the substrate in regions that should be unaffected by oxidation or even diffusion. In these areas within the substrate (not shown), the Laves phase decomposed into a Cr solid solution and Cr_3Ta_3N, indicating that the N derived from the manufacturing process and was present in the original base material (Figs. 4, 9).

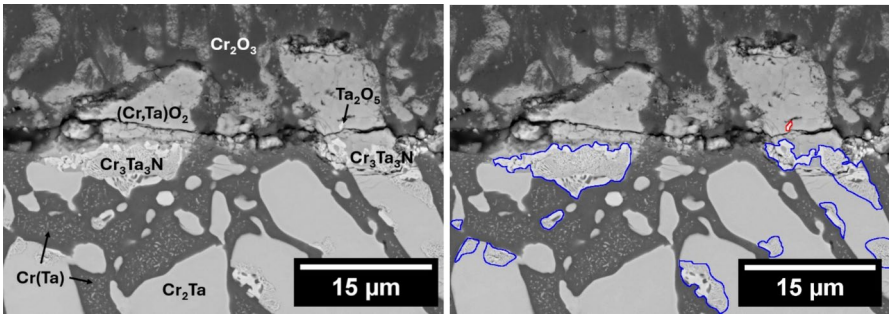

Fig. 9 SEM-BSE micrographs of the oxide layers of Cr-20 at.%Ta after oxidation and subsequent heat-treatment. On the right, the remaining Ta-oxide is highlighted in red, while the transformed Cr_3Ta_3N phase regions are blue. Oxidations was1000 °C for 48 h in Ar-2.5 vol.%O_2, with subsequent heat treatment in Ar at 1000 °C for 48 h

Post Oxidation Heat Treatment

To further investigate the thermodynamic stability of the thermally-grown oxides in contact with the substrate, some oxidized samples were heat-treated in an inert, high purity Ar atmosphere at 1000 °C for 48 h.

While the heat-treatment did not significantly alter the morphology of the oxides (Figs. 9, 10), EPMA-WDS compositional measurements and Raman spectroscopy revealed that the $CrTaO_4$ oxide completely transformed into $CrTa_2O_6$. EBSD, as shown in Fig. 11, did not reveal significant changes in the oxide morphology. Raman spectroscopy was used to clarify the local structure, identifying the $CrTaO_4$ specific peaks at 500 cm^{-1} and 770 cm^{-1} and $CrTa_2O_6$ specific peaks at 420 cm^{-1} and 680 cm^{-1}, as shown in Fig. 3 [30–32]. Additionally, a few remaining areas of N-rich transformed Laves phases were still present at the

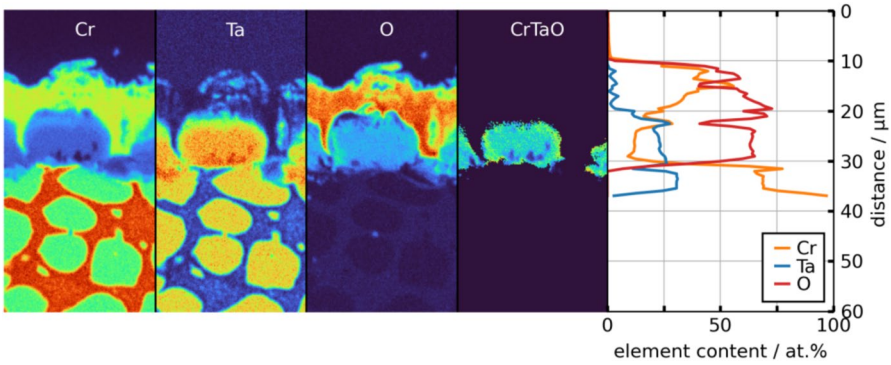

Fig. 10 EPMA-WDS elemental maps of the elements Cr, Ta and O as well as an overlay of these elements to highlight $(Cr,Ta)O_2$. A quantitative line scan shows the composition of the oxides on the right, indicating a composition of only $CrTa_2O_6$ after heat-treatment for 48 h at 1000 °C in Ar after oxidation at 1000 °C for 48 h in Ar-2.5 vol.%O_2

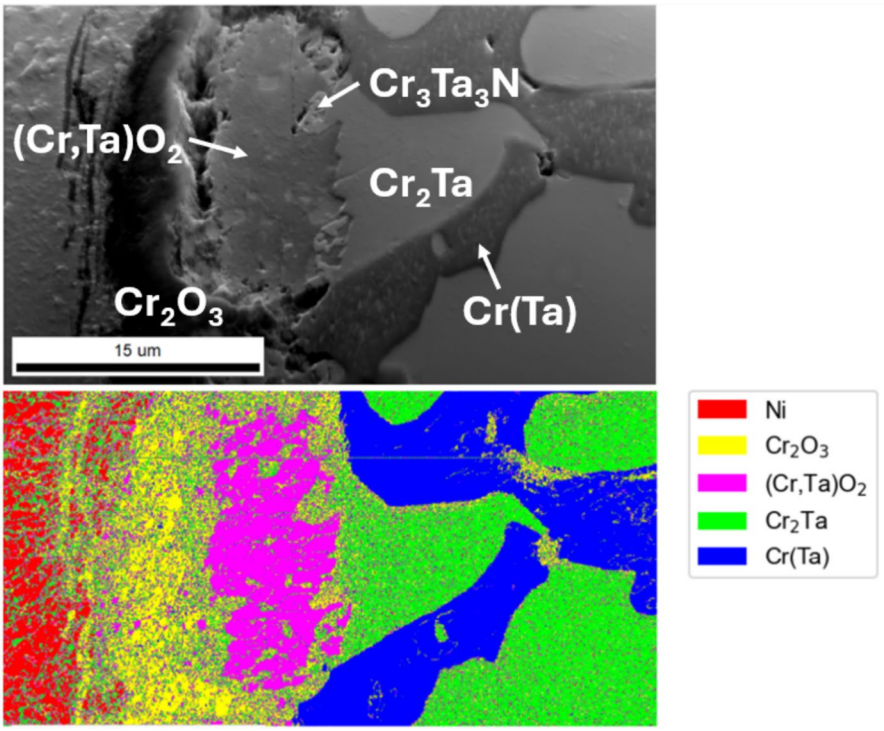

Fig. 11 SEM-SE and EBSD images of the oxide layer after oxidation (1000 °C for 48 h in Ar-2.5 vol.%O_2) plus heat treatment (1000 °C for 48 h in Ar). color-coded areas show the identified phases. $CrTaO_4$ and $CrTa_2O_6$ could not be differentiated via EBSD and are labeled as $(Cr,Ta)O_2$

oxide substrate interface and again matched the compositions of Cr_3Ta_3N and Ta_2O_5 with Cr(Ta) precipitations as can be seen in Fig. 12. In both cases, Cr diffused outwards and led to a significant depletion at the oxide-substrate interface, indicating that Cr was the main diffusing species during the heat-treatment.

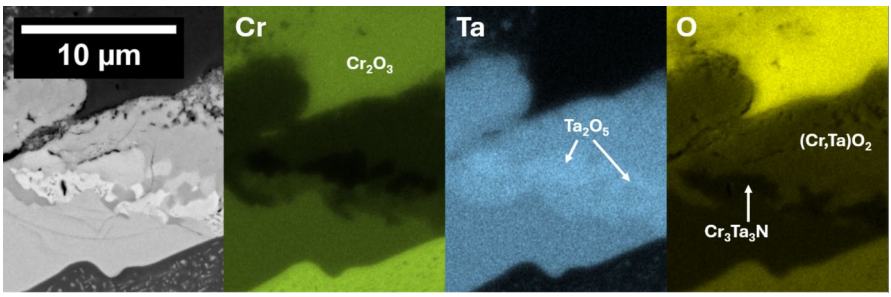

Fig. 12 High resolution BSE and EDS elemental maps of the oxide-substrate interface region showing Cr_3Ta_3N at the interface, Ta_2O_5 within the $(Cr,Ta)O_2$ and bordering the nitride after oxidation (1000 °C for 48 h in Ar-2.5 vol.%O_2) and heat treatment (1000 °C for 48 h in Ar)

Deeper within the material, in the zone unaffected by oxidation, the transformed Laves phase at the interface between the Cr solid solution and the Laves phase remained present or even grew after an additional 48 h at 1000 °C. This transformed phase further within the sample again shows the composition of Cr_3Ta_3N with Cr solid solution precipitates that also formed within the Cr_2Ta regions and is attributed to N present from the manufacturing process.

Fine Microstructure

The previous sections established the behavior of the Cr-20 at.%Ta alloy for a rather coarse microstructure on the order of 20–30 µm for the Laves phase and interdendritic Cr-channels in the range of 10 µm. For the finer microstructure, the characteristic spacing of the interdendritic Cr(Ta) and the size of Cr_2Ta intermetallics were reduced, see Fig. 13, promoting the formation of a continuous and more protective $(Cr,Ta)O_2$. It is well known that microstructure, dendrite size and phase distribution can strongly influence the scale morphology [17]. The ~ 2 g arc-melted samples led to a significantly finer dendrite size distribution than that of the ~ 100 g samples, with an average distance between C14 interdendritic regions of 2.1 µm, compared to the coarse sample with an average distance of 4.6 µm with occasional spacings up to 10 µm and thus a more homogenous distribution of the Laves phase.

The fine-grained samples exhibit the same two-phase microstructure as their coarse counterparts, consisting of the dendritic Cr_2Ta C14 hexagonal intermetallic Laves phase and the A2 body-centered cubic Cr(Ta) solid solution. However, the refined processing conditions result in a more uniform phase distribution with significantly reduced dendrite arm spacing. The phase compositions and volume fractions are similar to those observed in the coarse microstructure samples, maintaining the

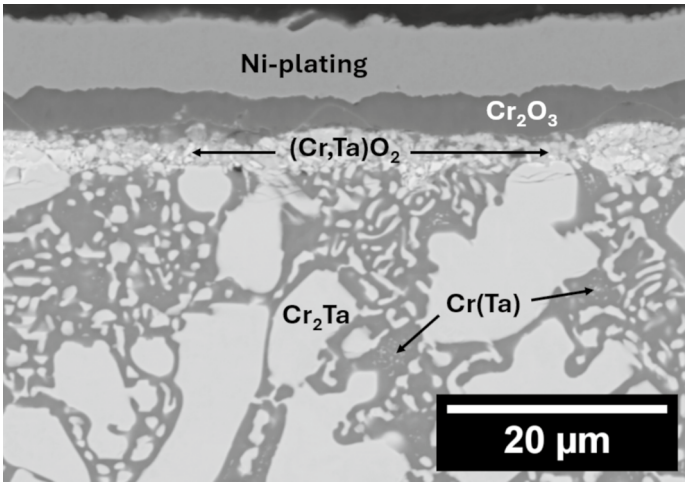

Fig. 13 Microstructure of the ~ 2 g arc melted button Cr-20 at.%Ta after oxidation (1000 °C for 48 h in Ar-2.5 vol.%O_2). Thea finer microstructure facilitates the formation of a continuous $(Cr,Ta)O_2$ layer over coarser-structured arc-melted samples of about 100 g

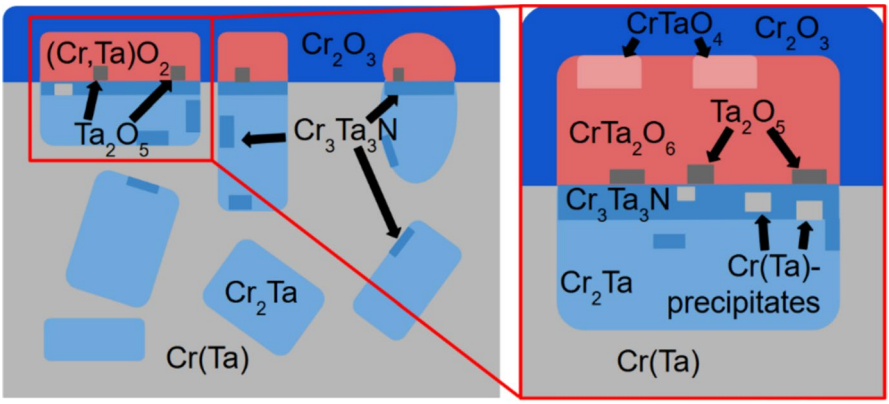

Fig. 14 Schematic illustration of the oxide scale after oxidation of Cr-20Ta and an enlarged illustration of the inset red rectangle. (1000 °C for 48 h in Ar-2.5 vol.%O_2)

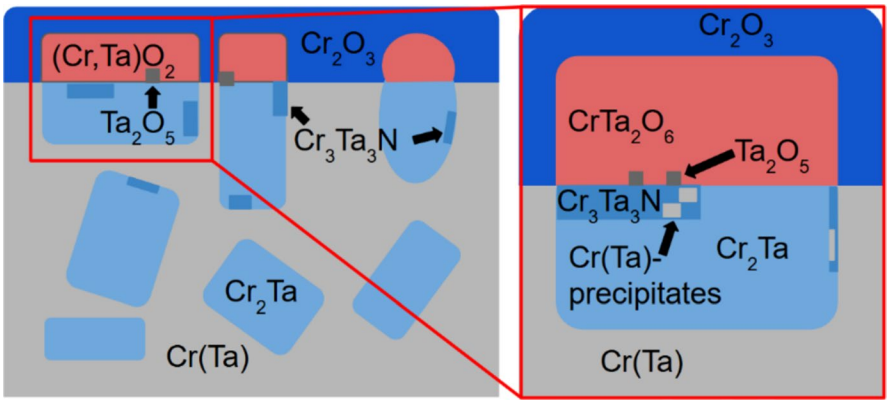

Fig. 15 Schematic illustration of the oxide scale of an oxidized and annealed Cr-20Ta sample and an enlarged illustration of the inset, representing 1000 °C for 48 h in Ar-2.5 vol.%O_2 and annealing at 1000 °C for 48 h in Ar

same overall alloy chemistry while achieving a more refined distribution. This finer microstructure fosters the formation of a continuous (Cr,Ta)O_2 layer at the oxide-substrate interface, which is covered by a continuous outer chromia layer as shown by cross-sectional SEM-BSE in Fig. 13. Unlike the coarse microstructure samples where (Cr,Ta)O_2 formation is limited to discrete regions above Laves phase dendrites, the fine microstructure enables lateral connectivity between adjacent (Cr,Ta)O_2 forming regions (Figs. 14, 15, 16). This continuity is achieved due to the reduced spacing between Laves phase regions, with the critical interdendritic spacing threshold being between 2 and 5 µm. As shown in Fig. 17, the fine microstructure samples exhibit a reduced total oxide thickness compared to coarse samples, demonstrating the protective effect of the continuous (Cr,Ta)O_2 layer.

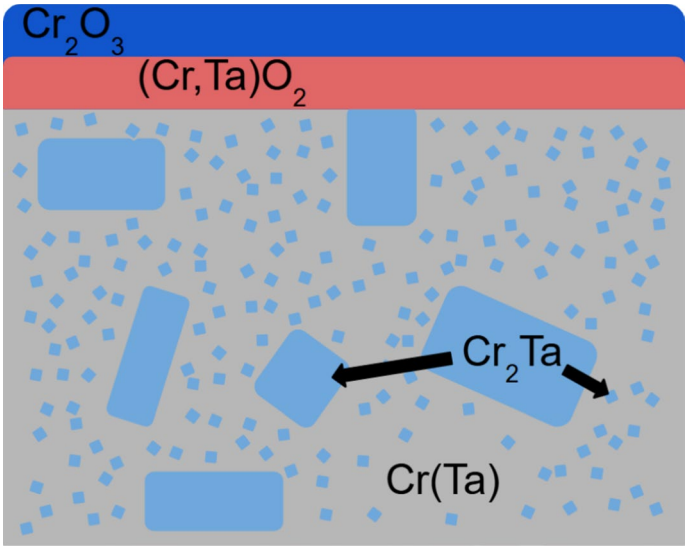

Fig. 16 Schematic illustration of the oxide scale of an oxidized Cr-20Ta sample with a finer microstructure. The fine microstructure enables continuous $(Cr,Ta)O_2$ formation after oxidation at 1000 °C for 48 h in Ar-2.5 vol.%O_2

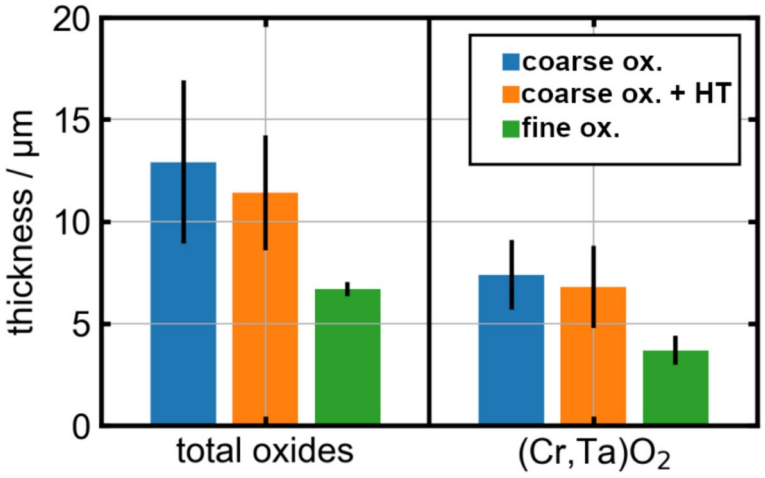

Fig. 17 Total oxide thickness and thickness of the $(Cr,Ta)O_2$ layer for coarse, oxidized + heat treated coarse and oxidized fine microstructure samples. (1000 °C for 48 h in Ar-2.5 vol.%O_2 and heat treatment at 1000 °C for 48 h in Ar)

The thermogravimetric analysis reveals distinct kinetic behavior for the fine microstructure samples compared to both the coarse Cr-20Ta and pure Cr samples. During the initial 3-h period, all samples show similar mass gain rates, indicating that the beneficial effect of $(Cr,Ta)O_2$ requires time to establish. After this initial

period, the fine microstructure samples demonstrate superior protective behavior with a transition to slower, parabolic kinetics. While the oxidation mechanisms were more easily observed in the coarser sample, this sample now allows a direct comparison with the kinetics of the pure chromia scale (Fig. 2). The influence of the continuous (Cr,Ta)O_2 on the kinetics lowers the oxidation kinetics by a factor of 8 for the parabolic growth constant compared to pure Cr, see Table 1.

Discussion

Despite attempts to use a simple system and environment, these results reveal the complexity of the oxidation behavior of the Cr-20 at.%Ta alloy, characterized by the formation of several distinct oxides. Additionally, the substantial impact of a finer or coarser microstructure on scale formation and its protective properties became obvious, while for both, the coarse and fine microstructure, Cr-20 at.%Ta alloys an outer Cr_2O_3 scale forms at the surface. This chromia scale appears to grow mainly by outward diffusion and oxidation from both the Cr(Ta) solid solution and the Cr_2Ta C14 Laves phase, which is consistent with observations in oxidation-resistant systems where similar complex oxides form [34, 35]. Below and within this Cr_2O_3 scale, EBSD, EPMA, and EDS confirmed the formation of (Cr,Ta)O_2 with two phases: $CrTa_2O_6$ and $CrTaO_4$, as schematically shown in Fig. 14. In areas that grow on a substrate with small precipitates of the intermetallic phase in the Cr-rich matrix, (Cr,Ta)O_2 is embedded within the outer Cr_2O_3 scale, once the region is oxidized. Whereas the (Cr,Ta)O_2 forms a continuous subscale on large Laves precipitates or when the Cr interdendritic solid solution matrix is sufficiently small, with a lateral spacing below a threshold between 2 and 5 µm as schematically shown in Fig. 16.

This smaller interdendritic spacing boosts continuous (Cr,Ta)O_2 formation by providing shorter diffusion pathsways from adjacent Ta-rich C14 regions, being the Ta-source. Such a fine distribution is necessary as Ta exhibits slow diffusion behavior [36]. Additionally, the finer phase distribution provides a larger amount of phase boundaries, which could act as oxygen diffusion pathways and oxide nucleation sites [37–40]. The exact threshold for interdendritic spacing that enables the transition from discrete to continuous (Cr,Ta)O_2 formation was estimated between 2 and 5 µm from the microstructures of this study. The fine-microstructure samples contain significantly larger C14 dendrites within the fine phase distribution, which not significantly affected the local oxidation rates. The oxide thickness exhibits a very low standard deviation, as shown in Fig. 17. Since $CrTaO_4$ is observed further out in the scale and $CrTa_2O_6$ nearer to the substrate, this spatial distribution supports the hypothesis that the scale growth is dominated by Cr outward diffusion, while Ta remains relatively stationary. As well as indicating, that $CrTa_2O_6$ is thermodynamically more stable than $CrTaO_4$. The strong influence of the microstructure is in line with Welch et al., who demonstrated that microstructural features, specifically the size and distribution of Cr- and Ta-rich precipitates, play a crucial role in forming continuous, protective layers that act as reservoirs supplying Cr cations to the growing scale [16, 22]. This behavior mirrors the oxidation processes observed in TaTiCr alloys [16, 35, 41], where microstructural factors, such as precipitate size

and distribution, significantly influence both the kinetics and stability of the oxide scales. Butler et al. showed a coarse distribution of Cr- and Ta- rich Laves phase leads to non-continuous, and thus less protective (Cr,Ta)O_2 [16, 22] and results in the conclusion that the (Cr,Ta)O_2 is most effective in combination with another oxide scale. This is confirmed in the current study and while the (Cr,Ta)O_2 growth kinetics could not be decoupled from the chromia kinetics, a significant reduction in the growth kinetics is achieved as shown in Fig. 2. These slower kinetics are confirmed by the calculated parabolic mass gain coefficient (Table 1) when the (Cr,Ta)O_2 formed, as is demonstrated for Cr-20 at.%Ta as compared to pure Cr (Table 1). Even the coarser microstructure samples demonstrate, for the first time, a quantitative difference in the scale growth between chromia and the (Cr,Ta)O_2 duplex layer. The positive influence of the (Cr,Ta)O_2 layer becomes obvious when comparing these results with the oxidation kinetics of other chromia forming alloys in similar reduced-oxygen partial pressure atmospheres at 1000 °C. Giggins et al. and Berthod et al. found parabolic rate constants for chromia forming alloys at 1000 °C between $\sim 3 * 10^{-6} \frac{g^2}{cm^4 h}$ and $\sim 1 * 10^{-7} \frac{g^2}{cm^4 h}$ which is in line with the parabolic rate constants found in this study for pure chromia [42, 43]. That supports the assumption that (Cr,Ta)O_2 is the reason for the reduced oxidation kinetics. (Cr,Ta)O_2 layers were suggested to be effective barriers to outward diffusion of cations before [4]. However, is has become clear, that inward diffusion of oxygen through the (Cr,Ta)O_2 layer is possible and lead to an oxygen diffusion zone and internal oxidation in Ti containing alloys that can dissolve oxygen in the substrate [4, 44]. Thus, the (Cr,Ta)O_2 layers protectiveness can be attributed to one main effect: Predominatly, a barrier to outward Cr-cation diffusion and Cr growth, but also secondly, a reduction of inward diffusion of oxygen. Only the finer microstructure lowered the oxidation kinetics on the whole sample surface, as demonstrated by the reduced scale thickness of samples with a finer dendrite distribution in addition to the lower mass gain, see Fig. 2. In the first 3 h, the growth rate is unaffected by the (Cr,Ta)O_2, meaning that the (Cr,Ta)O_2 subscale required time to establish (Fig. 13). Similar behavior was also observed in TaTiCr alloys, where oxidation kinetics transition to slower mass gain as continuous complex oxide layers, including (Cr,Ta,Ti)O_2 phases, develop [34, 35]. This can be seen in Fig. 2 for both Cr-20Ta alloys. Etienne et al. have also found that the oxidation resistance of Cr-Ta-Co alloys is directly related to the formation of (Cr,Ta)O_2 [34]. Bhowmik et al. have also shown a positive impact of Si additions on the Cr-Ta system, but since no protective silica was found the oxidation resistance was attributed to the formation of (Cr,Ta)O_2 [26].

Within the (Cr,Ta)O_2 scale, the sporadic presence of Ta_2O_5 was observed (Fig. 4). The eventual disappearance of $CrTaO_4$ after extended heat treatment also suggests that $CrTa_2O_6$ is the more stable oxide of the two (Cr,Ta)O_2, as predicted by thermodynamic calculations. The significant reduction of Ta_2O_5 after heat treatment also suggests $CrTa_2O_6$ to be more stable than Ta_2O_5. Using the software FactSage 5 (Database TANT) [28], the more stable oxide in these experimental conditions should be $CrTa_2O_6$ [28]. The calculations return values for the Gibb's free energy of formation at 1000 °C of **-1.0 MJ/molO_2** for $CrTa_2O_6$ and **-0.95 MJ/molO_2** for the Cr-richer $CrTaO_4$.

Interestingly, Ta_2O_5 has a predicted formation energy of **-0.84 MJ/molO_2**, making it thermodynamically less stable than $CrTaO_4$ and $CrTa_2O_6$.

In Fig. 14, a schematic illustration of the oxide scale of Cr-20Ta after oxidation at 1000 °C for 48 h is shown. The outermost oxide is chromia with (Cr,Ta)O_2 within the regions bordering the substrate above the Laves phase. In the outer area of the (Cr,Ta)O_2, the composition corresponds to $CrTaO_4$ while the inner composition is $CrTa_2O_6$. Besides this difference in the local chemical composition, Raman was able to differentiate these two oxides as they exhibit different peaks in the Raman spectrum, originating from the different chemical bonds within the crystal structure. The two crystal structures themselves proved too similar (rutile vs. trirutile) to be distinguished via XRD or EBSD At the substrate oxide interface, a transformed region with the composition Cr_3Ta_3N is visible with Cr(Ta) precipitates, but this is an artifact from residual N within the samples, since even deep in the substrate, local phase transformation (via Cr(Ta) precipitation) occurred to a more Ta-rich phase. STEM-EDS and diffraction analysis clearly identified this phase to contain around 15 at.% of nitrogen, matching the TEM diffraction patterns and chemical composition for Cr_3Ta_3N. The presence of nitrogen is unexpected as the arc-melting, heat treatment and oxidation exposures were performed in nitrogen-free atmospheres with residual nitrogen partial pressures of 4.9×10^{-6} bar. Therefore, it is most likely that nitrogen originated from contamination within the original raw material. This assumption is supported by thermodynamic calculations using the software FactSage 5 [28]. These calculations determine the residual nitrogen partial pressure in the manufacturing, oxidation and heat treatment atmospheres to be too low to form nitrides. Although the nitrogen-containing Cr_3Ta_3N phase is expected to modify the local diffusion behavior of Cr and O, its presence should derive from the manufacturing of the samples, but did not produce a detectable change in oxidation kinetics. Regions with and without C_3rTa_3N at the oxide-substrate interface showed similar oxide thicknesses, demonstrating that this phase does not significantly affect the oxidation rate under the conditions studied.

During the heat treatment, without further oxygen uptake, most of the Ta_2O_5 disappeared, ultimately merging into (Cr,Ta)O_2. During the subsequent heat treatment at 1000 °C for 48 h, further chromium diffuses outward, and excess oxygen in Ta_2O_5 reacts to (Cr,Ta)O_2 with the Laves phase at the oxide substrate interface (schematically shown in Fig. 15). Given the sluggish diffusion of tantalum, Ta does not migrate sufficiently outwards to form Ta oxides in the outer scale but instead transforms in the presence of chromium during homogenization to (Cr,Ta)O_2. Also, additional Cr_2Ta precipitates were observed in the Cr solid solution, indicating that the alloy does not reach the equilibrium state during the initial homogenization heat treatment. In the oxide, no $CrTaO_4$ was found after the aging heat treatment, again showing that $CrTa_2O_6$ is the thermodynamically more stable of the two (Cr,Ta)-oxides.

Conclusions

The oxidation behavior of binary Cr-20 at.%Ta alloy reveals complex mechanisms even in nitrogen-free environments, with significant improvements in oxidation resistance compared to pure chromium:

- Dual-phase $(Cr,Ta)O_2$ formation: Two distinct chromium-tantalum oxide phases form during oxidation—$CrTaO_4$ (rutile structure) in outer regions and $CrTa_2O_6$ (trirutile structure) closer to the substrate, with $CrTa_2O_6$ being thermodynamically more stable as confirmed by post-oxidation heat treatment.
- Microstructure-dependent oxidation kinetics: Fine-grained microstructures (2.1 µm average interdendritic spacing) enable continuous $(Cr,Ta)O_2$ layer formation, reducing the parabolic oxidation constant significantly compared to pure chromium. Even coarse-grained samples show significantly improved oxidation resistance despite non-continuous oxide formation.
- Chromium-dominated diffusion mechanism: Oxidation proceeds primarily through outward chromium diffusion from both Cr(Ta) solid solution and Cr_2Ta Laves phases, while tantalum remains relatively stationary, leading to the spatial distribution of $CrTaO_4$ (outer) and $CrTa_2O_6$ (inner) phases.
- Phase stability hierarchy: Thermodynamic calculations and experimental observations confirm the stability order from highest to lowest as **$CrTa_2O_6 > > CrTaO_4 > > Ta_2O_5$**, with Gibbs free energies of **-1.0 MJ/molO_2**, **-0.95 MJ/molO_2** and **-0.84 MJ/molO_2** respectively. $CrTaO_4$ completely transforming to $CrTa_2O_6$ during extended heat treatment at 1000 °C.
- Oxidation mechanism evolution: Initial oxidation (first 3 h) proceeds without significant $(Cr,Ta)O_2$ influence, followed by establishment of protective tantalum-containing subscales that transition the kinetics to a slower mass gain.
- Microstructural effects on continuity: Laves phase distribution and size critically influence $(Cr,Ta)O_2$ continuity; fine, homogeneously distributed Cr_2Ta phases (spacing threshold between 2 µm and 5 µm) promote continuous protective layers, while coarser distributions result in embedded, discontinuous oxide formation within the chromia scale.

Author Contributions F.L. wrote the main manuscript, prepared all figures and conducted all experiments except TEM analysis. TEM analysis was performed by M.D.. M.G., E.W., B.S., B.G.,C.T., C.S. suggested improvements, provided corrections and helped to interpret the results. All authors reviewed the manuscript.

Funding Open Access funding enabled and organized by Projekt DEAL. This work was funded by the Deutsche Forschungsgemeinschaft (DFG, German Research Foundation) under grant number 467750555.

Data Availability No datasets were generated or analysed during the current study.

Declarations

Competing interests The authors declare no competing interests.

References

1. Worch, H.: P. Kofstad, High Temperature Corrosion. Elsevier Applied Science, London/New York 1988, 546 Seiten mit 222 Illustr. und 6 Tabellen, £ 68.00, ISBN 1-85166-154-9. Cryst. Res. Technol. (1989). https://doi.org/10.1002/crat.2170240408
2. J.-W. Yeh, S.-K. Chen, S.-J. Lin, J.-Y. Gan, T.-S. Chin, T.-T. Shun, C.-H. Tsau, and S.-Y. Chang, *Advanced Engineering Materials* 2004. https://doi.org/10.1002/adem.200300567.
3. S. Schellert, B. Gorr, H.-J. Christ, C. Pritzel, S. Laube, A. Kauffmann, and M. Heilmaier, *Oxidation of Metals* 2021. https://doi.org/10.1007/s11085-021-10046-7.
4. F. Müller, B. Gorr, H.-J. Christ, J. Müller, B. Butz, H. Chen, A. Kauffmann, and M. Heilmaier, *Corrosion Science* 2019. https://doi.org/10.1016/j.corsci.2019.108161.
5. S. Schellert, B. Gorr, S. Laube, A. Kauffmann, M. Heilmaier, and H. J. Christ, *Corrosion Science* 2021. https://doi.org/10.1016/j.corsci.2021.109861.
6. S. Schellert, M. Weber, H. J. Christ, C. Wiktor, B. Butz, M. C. Galetz, S. Laube, A. Kauffmann, M. Heilmaier, and B. Gorr, *Corrosion Science* 2023. https://doi.org/10.1016/j.corsci.2022.110885.
7. O. N. Senkov, G. B. Wilks, D. B. Miracle, C. P. Chuang, and P. K. Liaw, *Intermetallics* 2010. https://doi.org/10.1016/j.intermet.2010.05.014.
8. O. N. Senkov, G. B. Wilks, J. M. Scott, and D. B. Miracle, *Intermetallics* 2011. https://doi.org/10.1016/j.intermet.2011.01.004.
9. H. Chen, A. Kauffmann, S. Seils, T. Boll, C. H. Liebscher, I. Harding, K. S. Kumar, D. V. Szabó, S. Schlabach, S. Kauffmann-Weiss, F. Müller, B. Gorr, H.-J. Christ, and M. Heilmaier, *Acta Materialia* 2019. https://doi.org/10.1016/j.actamat.2019.07.001.
10. D. B. Miracle and O. N. Senkov, *Acta Materialia* 2017. https://doi.org/10.1016/j.actamat.2016.08.081.
11. Y. F. Ye, Q. Wang, J. Lu, C. T. Liu, and Y. Yang, *Materials Today* 2016. https://doi.org/10.1016/j.mattod.2015.11.026.
12. C. Tang, B. Schäfer, C. Schroer, and B. Gorr, *Corrosion Science* 2025. https://doi.org/10.1016/j.corsci.2025.112847.
13. W. Ren, F. Ouyang, B. Ding, Y. Zhong, J. Yu, Z. Ren, and L. Zhou, *Journal of Alloys and Compounds* 2017. https://doi.org/10.1016/j.jallcom.2017.07.066.
14. Park, S.-J., Seo, S.-M., Yoo, Y.-S., Jeong, H.-W., Jang, H.: Materials (Basel, Switzerland) (2019). https://doi.org/10.3390/ma12182934
15. Li, M.H., Sun, X.F., Li, J.G., Zhang, Z.Y., Jin, T., Guan, H.R., Hu, Z.Q.: Oxidation of Metals (2003). https://doi.org/10.1023/A:1023604214245
16. N. J. Welch, T. M. Butler, M. J. Quintana, and P. C. Collins, *Journal of Alloys and Compounds* 2024. https://doi.org/10.1016/j.jallcom.2024.175613.
17. M. P. Brady, P. F. Tortorelli, and L. R. Walker, *Materials at High Temperatures* 2000. https://doi.org/10.1179/mht.2000.17.2.009.
18. M. P. Brady, J. H. Zhu, C. T. Liu, P. F. Tortorelli, and L. R. Walker, *Intermetallics* 2000. https://doi.org/10.1016/S0966-9795(00)00046-7.
19. M. P. Brady, J. H. Zhu, C. T. Liu, P. Tortorelli, L. R. Walker, C. G. McKamey, J. L. Wright, C. A. Carmichael, D. J. Larson, M. K. Miller, and W. D. Porter, *Materials at High Temperatures* 1999. https://doi.org/10.1179/mht.1999.018.
20. M. Brady, C. Liu, J. Zhu, P. Tortorelli, and L. Walker, *Scripta Materialia* 2005. https://doi.org/10.1016/j.scriptamat.2005.01.016.
21. A. Bhowmik, R. J. Bennett, B. Monserrat, G. J. Conduit, L. D. Connor, J. E. Parker, R. P. Thompson, C. N. Jones, and H. J. Stone, *Intermetallics* 2014. https://doi.org/10.1016/j.intermet.2013.11.002.

22. T. M. Butler, K. J. Chaput, J. R. Dietrich, and O. N. Senkov, *Journal of Alloys and Compounds* 2017. https://doi.org/10.1016/j.jallcom.2017.09.164.
23. M. P. Brady, J. H. Zhu, C. T. Liu, P. F. Tortorelli, J. L. Wright, and C. A. Carmichael, *Ultrahigh temperature intermetallic alloys* 1998. https://doi.org/10.2172/290926.
24. A. Bhowmik, C. N. Jones, I. M. Edmonds, and H. J. Stone, *Journal of Alloys and Compounds* 2012. https://doi.org/10.1016/j.jallcom.2012.03.070.
25. A. Bhowmik, K. M. Knowles, and H. J. Stone, *Intermetallics* 2012. https://doi.org/10.1016/j.intermet.2012.06.001.
26. A. Bhowmik, H. T. Pang, S. Neumeier, H. J. Stone, and I. Edmonds, *MRS Proceedings* 2011. https://doi.org/10.1557/opl.2011.38.
27. M. P. Brady, P. F. Tortorelli, E. A. Payzant, and L. R. Walker, *Oxidation of Metals* 2004. https://doi.org/10.1023/B:OXID.0000032330.95411.ec.
28. C. W. Bale, E. Bélisle, P. Chartrand, S. A. Decterov, G. Eriksson, A. E. Gheribi, K. Hack, I.-H. Jung, Y.-B. Kang, J. Melançon, A. D. Pelton, S. Petersen, C. Robelin, J. Sangster, P. Spencer, and M.-A. van Ende, *Calphad* 2016. https://doi.org/10.1016/j.calphad.2016.05.002.
29. J. Schindelin, I. Arganda-Carreras, E. Frise, V. Kaynig, M. Longair, T. Pietzsch, S. Preibisch, C. Rueden, S. Saalfeld, B. Schmid, J.-Y. Tinevez, D. J. White, V. Hartenstein, K. Eliceiri, P. Tomancak, and A. Cardona, *Natural Methods* 2012. https://doi.org/10.1038/nmeth.2019.
30. A. Jain, S. P. Ong, G. Hautier, W. Chen, W. D. Richards, S. Dacek, S. Cholia, D. Gunter, D. Skinner, G. Ceder, and K. A. Persson, *APL Materials* 2013. https://doi.org/10.1063/1.4812323.
31. M. Bagheri and H.-P. Komsa, *Scientific data* 2023. https://doi.org/10.1038/s41597-023-01988-5.
32. Bhardwaj, P., Singh, J., Kumar, R., Kumar, D., Verma, V., Kumar, R.: Appl. Phys. A (2022). https://doi.org/10.1007/s00339-021-05233-x
33. A. Soleimani Dorcheh and M. C. Galetz, *Oxidation of Metals* 2017. https://doi.org/10.1007/s11085-016-9685-1.
34. M. Louis Etienne, G. Stéphane, L. Guillaume, and M. Hideyuki, *Journal of Alloys and Compounds* 2023. https://doi.org/10.1016/j.jallcom.2022.167968.
35. N. J. Welch, M. J. Quintana, S. J. Kuhr, T. M. Butler, and P. C. Collins, *International Journal of Refractory Metals and Hard Materials* 2024. https://doi.org/10.1016/j.ijrmhm.2023.106437.
36. J. M. Leitnaker, M. G. Bowman, and P. W. Gilles, *Journal of the Electrochemical Society* 1961. https://doi.org/10.1149/1.2428137.
37. Sasidhar, K.N., Zhou, X.Y., Rohwerder, M., Ponge, D.: SSRN Journal (2022). https://doi.org/10.2139/ssrn.4295881
38. Z. Liu, Y. Zhang, X. Li, Y. Xu, X. Wu, C. Liu, X. Kong, C. Yao, and Z. Wang, *RSC Advances* 2021. https://doi.org/10.1039/d1ra00367d.
39. Krupp, U., Trindade, V.B., Schmidt, P., Christ, H.-J., Buschmann, U., Wiechert, W.: DDF (2005). https://doi.org/10.4028/www.scientific.net/DDF.237-240.946
40. Chepak-Gizbrekht, M.V., Knyazeva, A.G.: Evaluation of TiAl oxidation depth due to the grain boundary diffusion of oxygen. Izvestiya vuzov. Fizika (2024). https://doi.org/10.17223/00213411/67/1/6
41. N. J. Welch, M. J. Quintana, T. M. Butler, and P. C. Collins, *Journal of Alloys and Compounds* 2023. https://doi.org/10.1016/j.jallcom.2023.169000.
42. C. S. Giggins and F. S. Pettit, *Metallurgical Transactions* **1**, 1970 (1088). https://doi.org/10.1007/BF02811822.
43. P. Berthod, *Oxidation of Metals* **64**, 2005 (235). https://doi.org/10.1007/s11085-005-6562-8.
44. F. Lanoy, E. M. H. White, B. Schäfer, C. Tang, C. Schroer, B. Gorr, and M. C. Galetz, *Materials & Corrosion* 2025. https://doi.org/10.1002/maco.70070.

Authors and Affiliations

F. Lanoy[1] · E. M. H. White[1] · B. Schäfer[2] · C. Tang[2] · C. Schroer[2] · M. T. Duerrschnabel[2] · B. Gorr[2] · M. C. Galetz[1]

✉ F. Lanoy
fabian.lanoy@dechema.de

E. M. H. White
emma.white@dechema.de

B. Schäfer
bjoern.schaefer@kit.edu

C. Tang
chongchong.tang@kit.edu

C. Schroer
carsten.schroer@kit.edu

M. T. Duerrschnabel
michael.duerrschnabel@kit.edu

B. Gorr
bronislava.gorr@kit.edu

M. C. Galetz
mathias.galetz@dechema.de

[1] Dechema-Forschungsinstitut, Benzstrasse 1-3, 61352 Bad Homburg, Germany

[2] Institute of Applied Materials (IAM), Karlsruhe Institute of Technology (KIT), Kaiserstraße 12, 76131 Karlsruhe, Germany